ChemElectroChem

Chemistry Europe
European Chemical Societies Publishing

Accepted Article

Title: High Voltage Stability and Characterization of P2-Na0.66Mn1-yMgyO2 Cathode for Sodium-Ion Batteries

Authors: Tyler Or, Karthikeyan Kaliyappan, Zhengyu Bai, and Zhongwei Chen

To be cited as: *ChemElectroChem* 10.1002/celc.202000414

Link to VoR: https://doi.org/10.1002/celc.202000414

WILEY-VCH

10.1002/celc.202000414

High Voltage Stability and Characterization of P2-$Na_{0.66}Mn_{1-y}Mg_yO_2$ Cathode for Sodium-Ion Batteries

*Tyler Or[†], Dr. Karthikeyan Kaliyappan[†,‡], Prof. Zhengyu Bai[‡], and Prof. Zhongwei Chen[†,]**

[†]*Department of Chemical Engineering, University of Waterloo, 200 University Avenue West, Waterloo, Ontario N2L 3G1, Canada*

[‡]*School of Chemistry and Chemical Engineering, Key Laboratory of Green Chemical Media and Reactions, Ministry of Education, Henan Normal University, Xinxiang, 453007 China*

***Corresponding author:** Dr. Zhongwei Chen (zhwchen@uwaterloo.ca)

KEYWORDS

Mg doping, P2-O2, P2-OP4, P2-type cathode, phase transition

Abstract

The development of sodium-ion batteries is currently limited by the availability of high-energy and low-cost cathode materials. The energy density of cathodes can be maximized by expanding the voltage range for cycling, but this often leads to severe capacity degradation. Cathodes that demonstrate good long-term cyclability at high voltage cut-offs (> 4.3 V *vs* Na/Na^+) are scarce in the literature. In this work, layered P2-$Na_{0.66}Mn_{1-y}Mg_yO_2$ was synthesized using a modified Pechini method at various compositions (y = 0, 0.05, 0.1) and characterized after extended cycling between 2 – 4.5, 4.6, and 4.7 V *vs* Na/Na^+. $Na_{0.66}Mn_{0.95}Mg_{0.05}O_2$ displayed a similar initial discharge capacity to $Na_{0.66}MnO_2$ with significant improvements in cycle retention. It was most promising when cycled between 2 – 4.5 V, retaining 140 mAh g^{-1} (82% retention) and 116 mAh g^{-1} (68% retention) after 50 and 100 cycles respectively at low current (40 mA g^{-1}). A higher Mg dopant quantity led to improvements in cyclability and rate performance albeit with lower initial discharge capacity. Electrochemical and physical (*ex-situ* XRD) characterizations were used to delineate the role of high-voltage phase transitions, SEI layer formation, electrolyte solvent insertion into sodium slabs, and active material degradation/dissolution toward capacity loss.

Introduction

The increasing global demands for energy necessitate technological advancements in clean energy storage. Current energy generation relies on fossil fuels, which are inherently finite, release carbon dioxide into the atmosphere, and are limited in geographic distribution. Lithium-ion battery (LIB) technology is the current state-of-the-art due to their unmatched energy and power density. However, increasing demands for LIBs will constrain natural lithium resources and increase prices, which poses problems for their widespread adoption in electric vehicles and grid energy storage.[1]

Sodium-ion batteries (SIBs) are an emerging technology that has been proposed as an alternative to LIBs due to the low cost and abundance of sodium and their similar (de)intercalation chemistry. SIBs are most promising for use in large-scale grid storage applications, where cost and raw material abundance are particularly important.[2] However, while the raw material cost of sodium-based cathodes is lower than their lithium-based counterparts, the energy density of SIBs is inherently limited because of the low intercalation potential of the cathodes. Furthermore, in comparison to LIBs, SIBs demonstrate considerably poorer cycle retention.[3] This is because SIB cathodes experience structural evolution over repeated (de)intercalation of Na^+ with the host structure due to the large ionic radius of Na^+ (1.02 Å) compared to Li^+ (0.76 Å). Thus, to fully realize the potential of SIBs in large-scale storage, cathode materials comprised of low-cost, abundant, and nontoxic materials that can deliver high energy and power output are required.

Layered transition metal oxides (Na_xMO_2, M = Co, Fe, Ni, Ti, V, Cr, and/or Mn, $x = 0.6 – 1$) are a common class of cathode materials known for their high electrochemical stability and rate performance. They are often classified as O3 or P2-type, which refers to the geometry of the sodium site (octahedral vs. trigonal prismatic) and the number of transition metal oxide layers in the unit cell.[4] In general, P2-type cathodes have a lower sodium content but are more structurally stable and resist phase changes during the charge/discharge process, thus resulting in a higher discharge capacity (with Na-metal foil as the counter electrode) and cycle stability. Furthermore, P2-type cathodes demonstrate favorable diffusion kinetics for Na^+ due to the preferred prismatic coordination of the relatively large Na^+ ions.[5] Although P2-type cathodes may possess a high theoretical capacity, they must be cycled at high voltage cut-offs ($V_{cut\text{-}off}$, >4.4 V *vs* Na/Na^+) in order to exploit this and maximize their energy density. However, extending $V_{cut\text{-}off}$ can severely compromise cathode cyclability due to irreversible phase and volume changes, active material degradation and dissolution, and uncontrolled electrolyte side reactions. Cathodes that demonstrate good cyclability at high $V_{cut\text{-}off}$ are scarce in the literature.

P2-Na_xMnO_2 is a promising SIB cathode composition due to its abundance, environmental benignity, low cost, and high theoretical (243 mA h g^{-1}) and reported discharge capacity from the Mn^{3+}/Mn^{4+} redox.[6–8] However, this material often displays a drastically poor cycle stability, which is caused by the presence of Jahn-Teller distorted Mn^{3+} ions, coupled with phase changes from the insertion and extraction of Na^+ ions, thus leading to structural degradation throughout cycling. In order to improve the performance of P2-Na_xMnO_2, Mn can be partially substituted with Mg (P2-$Na_xMn_{1-x}Mg_xO_2$, $0 \leq x \leq 0.2$). Adding Mg as a dopant has been found to improve cycle stability by reducing the amount of Mn^{3+},[8,9] enhancing the rate performance,[10–12] and generating smooth charge/discharge curves which implies the suppression of phase changes. Mg can partially substitute the Na^+ sites and serve as a 'pillar' to stabilize the structure and suppress Na^+/vacancy ordering.[13,14] In general, increasing the amount of Mg dopant improves the cycle stability at the expense of the discharge capacity, as Mg is electrochemically inactive. However, one study reported an anomalous case with P2-$Na_{2/3}Mn_{0.72}Mg_{0.28}O_2$, which demonstrated a high initial discharge capacity (~220 mA h g^{-1}) at 10 mA g^{-1} when cycled from 1.5 – 4.4 V *vs* Na/Na^+ albeit with poor cycle stability and large voltage hysteresis.[15] This was explained by the large quantity of Mg^{2+}, which activates the oxide ions to participate in redox as evidently seen in the unique and pronounced plateau at 4.2 V in the charge curve. The oxide redox mechanism in this compound was confirmed by Maitra *et al.*, who also suggested that Mg^{2+} in the transition metal oxide layer could help suppress oxygen evolution, in contrast to that observed in cation-disordered rock salt structures.[16] Nevertheless, very few studies have demonstrated and characterized the performance of P2-$Na_xMn_{1-y}Mg_yO_2$ in the high voltage region,[9,17] which is important

to improve the energy density of the material, whereas most studies have characterized the material at a ≤ 4.0 $V_{cut-off}$.[8,10,18]

In this work, P2-$Na_{0.66}Mn_{1-y}Mg_yO_2$ was synthesized using a modified Pechini process at three Mg dopant quantities, y = 0, 0.05, and 0.01 and systematically characterized at $V_{cut-off}$ of 4.5, 4.6, and 4.7 V. The long-term capacity retention (over 75 – 100 cycles) and rate performance were assessed for each composition through galvanostatic charge-discharge characterization. Mechanisms of capacity fade were assessed via post-cycling EIS and *ex-situ* XRD characterization.

Results and Discussion

$Na_{0.66}Mn_{1-y}Mg_yO_2$ was synthesized using a modified Pechini method at two compositions with target stoichiometries of $Na_{0.66}Mn_{0.95}Mg_{0.05}O_2$ and $Na_{0.66}Mn_{0.9}Mg_{0.1}O_2$. In this technique, the metal ion precursors are dissolved in dilute HNO_3(aq) and mixed with citric acid and PEG. The metal ions form coordination complexes with citric acid while PEG grafts onto the citric acid through an esterification reaction, forming a polymeric resin where cations are uniformly distributed. Following calcination and decomposition of the polymer matrix, the ceramic particles produced typically possess a smaller and more uniform size compared to conventional sol-gel methods.[19–21] The synthesized compositions were confirmed using ICP-AES with resulting Mg/Mn ratios of 0.0512 and 0.115 respectively. SEM images of the particles are shown in Figure S1C-D. Both compositions display an identical plate-like particle morphology with sizes ranging from 1 – 3 μm, which is typically observed in P2-layered structures. In comparison, the same composition was synthesized using a conventional citric-acid assisted sol-gel method using identical sintering conditions. SEM images of the resultant particles (Figure S1A-B) appear larger with a more heterogeneous size distribution (2 – 5 μm). The benefits of having a smaller and uniform particle size toward electrochemical performance are well established – the higher surface area can increase the availability of electrochemical reaction sites and improve the interparticle contact, thus improving electronic conductivity and capacity, while also shortening the solid-state diffusion length for Na^+.[22] Thus, $Na_{0.66}Mn_{1-y}Mg_yO_2$ synthesized using the modified Pechini method was used for further physical and electrochemical characterization.

The powder XRD patterns (Figure 1) show that $Na_{0.66}Mn_{1-y}Mg_yO_2$ formed a phase-pure P2-layered material with a hexagonal lattice indexed to the $P6_3/mmc$ space group. The hexagonal lattice parameters were obtained using a Rietveld refinement (Table S1), yielding a = 2.888 Å and c = 11.314 Å for y = 0.1, and a = 2.882 Å and c = 11.281 Å for y = 0.05. The lattice parameters increase with higher Mg^{2+} substitution due to Mg^{2+} having a larger ionic radius compared to Mn^{3+}/Mn^{4+}.[23] The larger c-axis lattice parameter implies

an expanded interlayer space for the y = 0.1 composition, which can improve Na^+ diffusion kinetics and facilitate the reversibility of potential phase changes. It should be noted that no superlattice peaks that may correspond to Na^+/vacancy or $Mn^{3+}/Mn^{4+}/Mg^{2+}$ ordering were observed in the patterns.[8,9]

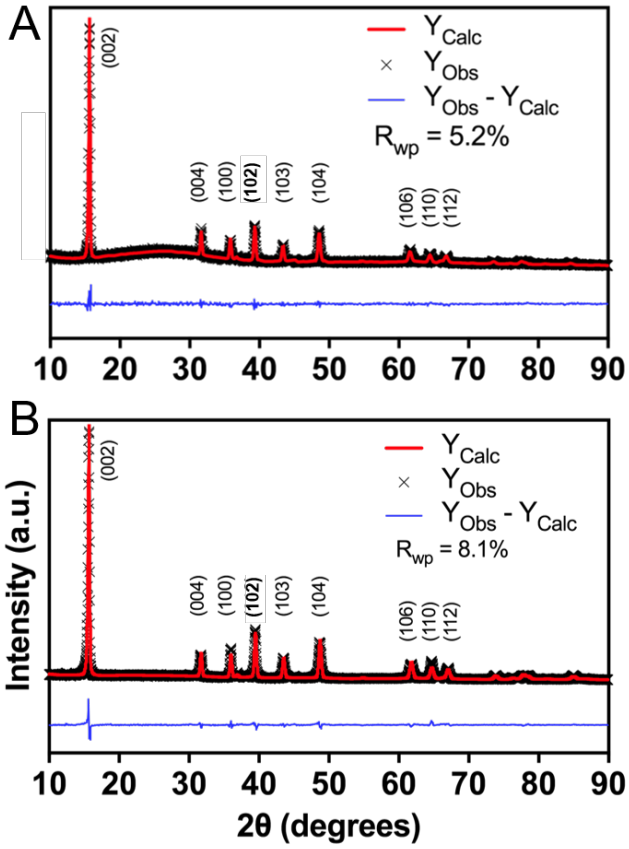

Figure 1. Refined XRD patterns of pristine P2-$Na_{0.66}Mn_{1-y}Mg_yO_2$. A) y = 0.1, R_{wp} = 5.2% B) y = 0.05, R_{wp} = 8.1%

$Na_{0.66}Mn_{1-y}Mg_yO_2$ Electrochemical Performance

The galvanostatic charge-discharge performance results are summarized in Table 1 below and Table S2 in the SI. The initial charge-discharge curves of $Na_{0.66}Mn_{0.95}Mg_{0.05}O_2$ at various $V_{cut\text{-}off}$ are shown in Figure 2A, which appear significantly smoother compared to our synthesized $Na_{0.66}MnO_2$ (Figure S2). As clearly shown in the dQ/dV plots (Figure S3), the peaks appearing from 2.1 – 2.4 V *vs* Na/Na^+ for $Na_{0.66}Mn_{0.95}Mg_{0.05}O_2$ correspond to the Mn^{3+}/Mn^{4+} redox reaction while the 3.0 – 3.5 V peaks are ascribed to a reversible P2-OP4 phase transition.[11] This transition occurs when Na^+ is extracted from large prismatic sites within the P2 phase with 'AB BA' stacking. As Na^+ is extracted, adjacent transition metal oxide slabs repel electrostatically, which generally corresponds with an expansion of the *c*-axis lattice parameter and shrinking of the *a* parameter.[24] With further extraction, the process is also associated with slab gliding for

energetic balance, forming octahedral vacancies that shrink the interlayer spacing. The stacked-fault OP4 phase is an intermediate transition occurring ~3.5-3.6 V where every other prismatic layer is converted into an octahedral layer with 'AB BA CB BC' stacking. At ~4.2 – 4.3 V, the prismatic sites may convert entirely to octahedral sites, resulting in an O2 phase with 'ABC BAB' stacking. The formation of this phase is clearly observed in compositions such as P2-$Na_{2/3}Ni_{1/3}Mn_{2/3}O_2$.[24] The O2 phase transition is not as reversible as the OP4 transition and is a significant reason for capacity fade when cycling at high $V_{cut\text{-}off}$ ranges. The benefits of Mg^{2+} doping in P2 cathodes has been characterized in prior work.[25,26] Mg^{2+} can suppress and delay the onset OP4 and P2 phase transition by allowing more Na^+ ions to reside in prismatic sites during charging. For Mn-rich cathodes, Mg^{2+} doping can significantly improve the cycle retention as it not only delays the OP4 and P2 phase transition, but also increases the average ionicity of Mn, and thus suppresses ordering effects and structural changes associated with Jahn-Teller distorted Mn^{3+} ions. This corresponds to much smoother-appearing charge-discharge curves for the Mg-doped samples. While our synthesized $Na_{0.66}MnO_2$ possessed a distinct oxidation peak at 4.22 V (Figure S2B), this was not observed in $Na_{0.66}Mn_{0.95}Mg_{0.05}O_2$ (Figure S3), confirming that Mg doping suppressed/delayed the P2-O2 phase transition. The smoothing of plateaus appearing below 4.0 V also implies that Mg substitution suppressed Na^+/vacancy ordering.[27] Both samples displayed a distinct peak when charged to ~4.7 V, suggesting that Na^+ extraction was strained at this $V_{cut\text{-}off}$ and likely approached the theoretical limit.

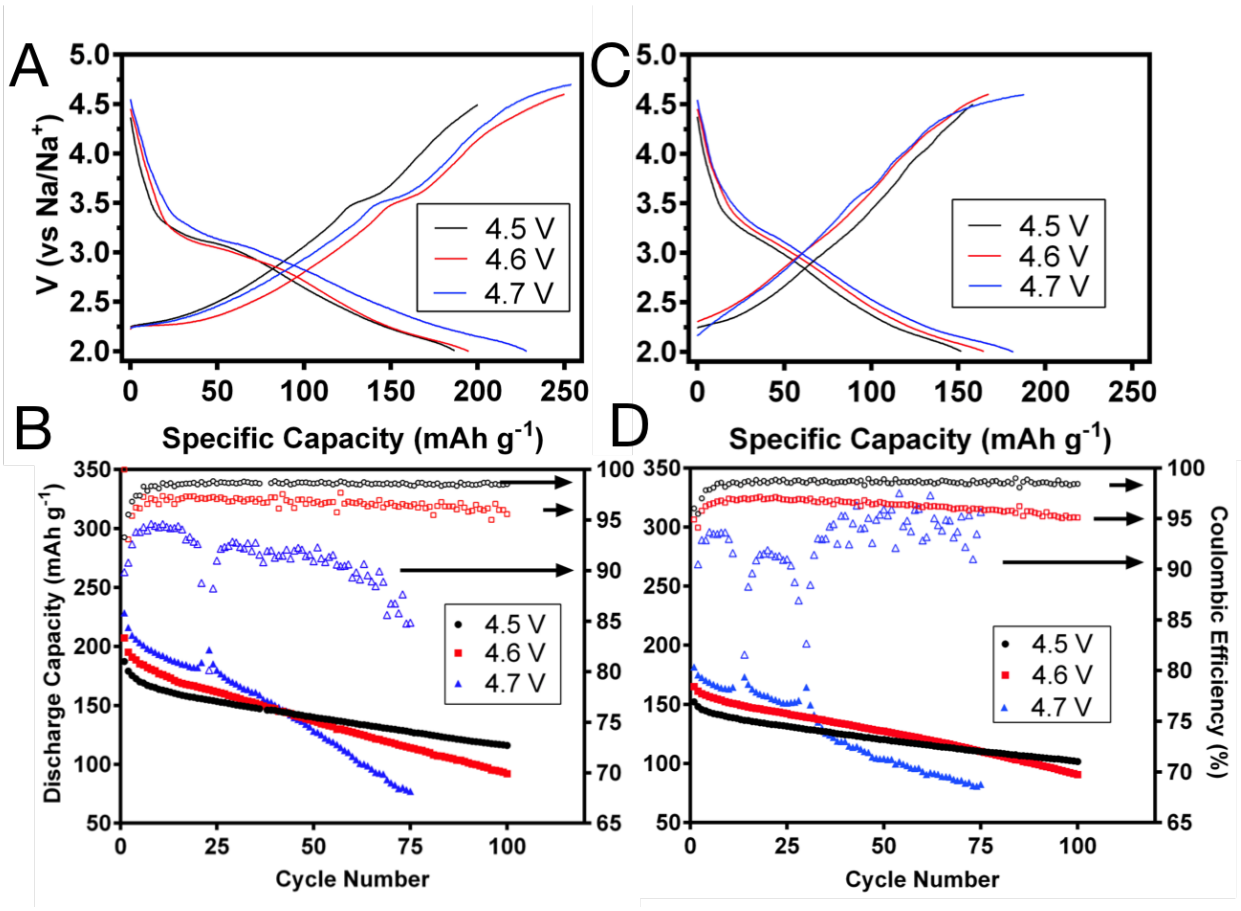

Figure 2. Initial galvanostatic charge-discharge curves (A and C) and cycle stability (B and D) for $Na_{0.66}Mn_{1-y}Mg_yO_2$, y = 0.05 (A and B) and y = 0.1 (C and D) cycled at 40 mA g^{-1} and at 4.5, 4.6, and 4.7 $V_{cut\text{-}off}$.

Electrochemical performance of our synthesized Mg-doped cathodes was characterized at three upper $V_{cut\text{-}off}$: 4.5, 4.6, and 4.7 V. The initial discharge capacity and cycle stability were assessed at a low current of 40 mA g^{-1}. As expected, the initial discharge capacity increased with respect to $V_{cut\text{-}off}$ due to the increased Na^+ extraction, but this came at the expense of poorer capacity retention. It is well understood that at high $V_{cut\text{-}off}$, cyclability is reduced substantially due to 1) irreversible changes in the bulk structure (*e.g.*, slab gliding and Na^+/vacancy ordering), 2) extensive decomposition of electrolyte resulting in increased interfacial resistance due to unstable solid-electrolyte-interphase (SEI) layer growth, 3) solvent insertion within the interlayer space of transition metal oxide slabs, and 4) active material dissolution and particle/electrode pulverization from extensive cycling.[28] These factors for capacity degradation are examined in subsequent sections. It is interesting to note that $Na_{0.66}Mn_{0.95}Mg_{0.05}O_2$ displayed a similar initial discharge capacity (Table 1) compared to our synthesized $Na_{0.66}MnO_2$ (Table S2); however, the 5% substitution of Mn^{3+}/Mn^{4+} with Mg^{2+} enhanced the cycle retention significantly. When cycling between 2

– 4.5 V, the capacity retention of $Na_{0.66}Mn_{0.95}Mg_{0.05}O_2$ was promising, retaining 140 mAh g^{-1} (82%) and 116 mAh g^{-1} (68%) after 50 and 100 cycles respectively. Table S3 compares this capacity retention to other layered oxide cathodes in the literature cycled at a similar voltage range and current. Cycle stability enhancement was more pronounced at higher $V_{cut\text{-}off}$, for instance $Na_{0.66}Mn_{0.95}Mg_{0.05}O_2$ retained 50% of its discharge capacity after 100 cycles between 2 – 4.6 V, whereas $Na_{0.66}MnO_2$ decayed to 23%. At 4.7 $V_{cut\text{-}off}$, the initial discharge capacity of $Na_{0.66}Mn_{0.95}Mg_{0.05}O_2$ (229 mAh g^{-1}) is among the highest ever reported for a sodium layered metal oxide[29] – it should be noted that despite the low average discharge potential (~2.7 V), this still corresponds to an ultra-high energy density of 616 Wh kg^{-1}. However, cycle stability was drastically poorer, retaining 38% capacity after 75 cycles. Figure S4 shows the evolution of the charge-discharge curves over 100 cycles at the various $V_{cut\text{-}off}$. It is evident that voltage polarization increased with respect to $V_{cut\text{-}off}$ and cycle number. However, the shape of the curves at 4.5 and 4.6 $V_{cut\text{-}off}$ remained similar, whereas at 4.7 $V_{cut\text{-}off}$, a severe shrinkage of the smooth plateau from 2 – 3.25 V was observed. This suggests that active material dissolution/degradation was a significant factor for capacity loss. It is understood that the Jahn-Teller distorted Mn^{3+} ion can undergo a disproportionation reaction to form Mn^{4+} and Mn^{2+}, where Mn^{2+} is known to dissolve in carbonate-based liquid electrolytes.[30] The charge curve plateaus at ~4.7 V that are evident after the initial cycles indicate that Na^+ extraction was strained at this $V_{cut\text{-}off}$, likely due to irreversible phase changes that restrict Na^+ diffusion. The capacity contribution from the plateaus likely corresponds to electrolyte decomposition, which is reflected by the low coulombic efficiency.

On the other hand, the charge-discharge curves of $Na_{0.66}Mn_{0.9}Mg_{0.1}O_2$ showed no peaks from 3.0 – 3.5 V, suggesting that the P2-OP4 phase transition was suppressed due to the higher quantity of Mg dopant. As expected, the initial discharge capacity was suppressed compared to $Na_{0.66}Mn_{0.95}Mg_{0.05}O_2$, whereas the cycle stability improved. The improvement was more notable when cycled at higher $V_{cut\text{-}off}$, supporting the claim that Mg delays and suppresses irreversible high-voltage phase transitions. A stability comparison among the compositions (y = 0, 0.05, 0.1) is shown in Figure S5. At 4.5 $V_{cut\text{-}off}$, $Na_{0.66}Mn_{0.95}Mg_{0.05}O_2$ and $Na_{0.66}Mn_{0.9}Mg_{0.1}O_2$ have a similar trend in cycle stability. However, at 4.6 and 4.7 $V_{cut\text{-}off}$, the two compositions reach the same discharge capacity after ~100 and 73 cycles respectively. Thus, the energy density and long-term cyclability of $Na_{0.66}Mn_yMg_{1-y}O_2$ can be maximized at y = 0.05 and using a 4.5 $V_{cut\text{-}off}$.

The rate performance of both Mg-doped compositions is shown in Figure 3. An interesting trend is noted where the discharge capacity is throttled at high current when cycled at high cut-off voltages. At a 4.5 $V_{cut\text{-}off}$, $Na_{0.66}Mn_{0.95}Mg_{0.05}O_2$ retained 63% of its discharge capacity when ramped from 50 to 333 mA g^{-1}, while 51% and 53% capacity retentions were observed at 4.6 and 4.7 $V_{cut\text{-}off}$ respectively. Similarly,

$Na_{0.66}Mn_{0.9}Mg_{0.1}O_2$ retained 65%, 62%, and 53% of its discharge capacity at 4.5, 4.6, and 4.7 $V_{cut\text{-}off}$ respectively at the same current density range. A similar trend was observed by Buchholz *et al.* when comparing the rate capability of $Na_xMn_{0.89}Mg_{0.11}O_2$ at 4.4 and 4.6 $V_{cut\text{-}off}$.[9] This effect is ascribed to the kinetic unfavorability of the high-voltage phase transitions, which is supported by the fact that our synthesized $Na_{0.66}Mn_{0.9}Mg_{0.1}O_2$ greatly outperformed $Na_{0.66}Mn_{0.95}Mg_{0.05}O_2$ at a 4.6 $V_{cut\text{-}off}$. It is understood that there is a high energy barrier for Na^+ diffusion through the octahedral sites that form at high voltages, due to strong Coulombic repulsion between Na^+ and the metal oxide layers.[31] The improved rate capability of $Na_{0.66}Mn_{0.9}Mg_{0.1}O_2$ can also be ascribed to its expanded *c*-axis lattice parameter, which enables facile diffusion of Na^+ in the interlayer spacing.[32] Furthermore, reducing the amount of Jahn-Teller active ions and Na^+/vacancy ordering by increasing the Mg dopant has a significant impact toward reducing the energy barrier for Na^+ diffusion.[33]

Post-Cycling Characterization

The EIS spectra of the electrodes after 100 cycles at 40 mA g^{-1} were obtained to study the interfacial properties of the electrodes at various conditions. The Nyquist plots of $Na_{0.66}Mn_{0.95}Mg_{0.05}O_2$ cycled at 4.5 and 4.6 $V_{cut\text{-}off}$ show a semicircle at the high-medium frequency region followed by a straight incline at low frequency, which correspond to the electrode/electrolyte charge-transfer impedance (R_{ct}) and Warburg impedance (W) respectively. Figure 3C shows that R_{ct} increases substantially when cycled at higher $V_{cut\text{-}off}$, which reflects the poor kinetics likely associated with irreversible phase changes and structural degradation at high $V_{cut\text{-}off}$. With extensive cycling at 4.7 $V_{cut\text{-}off}$, a new overlapped semicircle appears at the high-frequency region, which is ascribed to a Na^+ migration impedance (R_f) through the surface of the electrode. This likely arises from the formation of a thick SEI layer due to significant decomposition of the carbonate-based electrolyte at this $V_{cut\text{-}off}$.[27] The magnitudes of R_f and R_{ct} are substantial after cycling at 4.7 $V_{cut\text{-}off}$ – Table S4 shows the calculated impedance values from curve fitting based on the equivalent circuit shown as an inset of Figure 3C. For comparison, $Na_{0.66}Mn_{0.9}Mg_{0.1}O_2$ cycled at 4.5 $V_{cut\text{-}off}$ displayed a similar R_f and R_{ct} to $Na_{0.66}Mn_{0.95}Mg_{0.05}O_2$. However, when cycling at 4.7 $V_{cut\text{-}off}$, the sample with the higher Mg content displayed a considerably lower R_f and R_{ct}. These results indicate that SEI layer growth is a significant factor for capacity loss at 4.7 $V_{cut\text{-}off}$, and also support the fact that Mg substitution can suppress irreversible high-voltage phase changes, resulting in improved capacity retention and kinetics.

Table 1. Summary of electrochemical performance benchmarks of $Na_{0.66}Mn_{1-y}Mg_yO_2$ cycled at various voltage ranges.

	Voltage Range	$Na_{0.66}Mn_{0.9}Mg_{0.1}O_2$	$Na_{0.66}Mn_{0.95}Mg_{0.05}O_2$
Initial Discharge Capacity (mAh g^{-1}) at 40 mA g^{-1}	2 – 4.5 V	152	187
	2 – 4.6 V	165	207
	2 – 4.7 V	182	229

Capacity Retention at 40 mA g^{-1}	2 – 4.5 V (100 Cycles)	71%	68%
	2 – 4.6 V (100 Cycles)	58%	50%
	2 – 4.7 V (75 Cycles)	49%	38%
Coulombic Efficiency (Cycle 5)	2 – 4.5 V	98.5%	98.7%
	2 – 4.6 V	96.4%	96.2%
	2 – 4.7 V	93.7%	93.8%
Discharge Capacity at 50, 83, 167, 250, and 333 mA g^{-1} respectively	2 – 4.5 V	145, 136, 120, 105, and 94 mAh g^{-1}	177, 159, 142, 125, and 112 mAh g^{-1}
	2 – 4.6 V	159, 142, 124, 109, and 98 mAh g^{-1}	196, 168, 134, 113, and 99 mAh g^{-1}
	2 – 4.7 V	175, 153, 130, 108, and 93 mAh g^{-1}	204, 179, 154, 129, 108 mAh g^{-1}

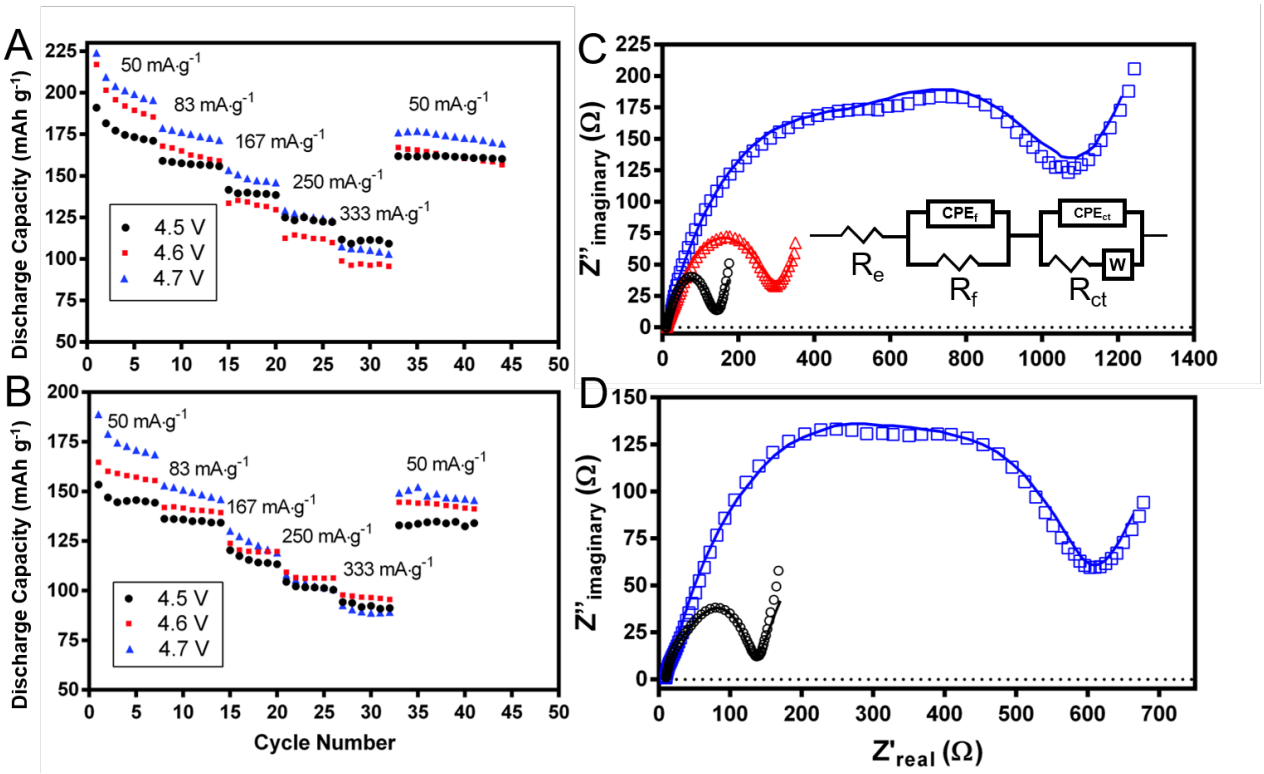

Figure 3. Rate performance of A) $Na_{0.66}Mn_{0.95}Mg_{0.05}O_2$ and B) $Na_{0.66}Mn_{0.9}Mg_{0.1}O_2$. EIS spectra after 100 cycles. Symbols represent the data point while solid lines show the fitted spectra. C) $Na_{0.66}Mn_{0.95}Mg_{0.05}O_2$ cycled at $V_{cut\text{-}off}$ of 4.5 V (black), 4.6 V (red), and 4.7 V (blue). D) $Na_{0.66}Mn_{0.9}Mg_{0.1}O_2$ cycled at $V_{cut\text{-}off}$ of 4.5 V (black) and 4.7 V (blue).

In order to study the structural stability of $Na_{0.66}Mn_{0.9}Mg_{0.1}O_2$ and $Na_{0.66}Mn_{0.95}Mg_{0.05}O_2$, samples were characterized via *ex-situ* XRD at various stages of cycling from 2 – 4.5 V. Figure 4 reveals that for both compositions, the P2 structure was retained throughout cycling, with no discernible shifts in peak position and intensity ratio. Even the XRD pattern at 4.5 V (first charge) showed no peaks associated with the

octahedral phase, which confirms that Mg doping suppresses/delays the P2-O2/OP4 phase transition and explains the smoothened charge-discharge profile and better capacity retention. Formation of the octahedral phase is typically observed in desodiated P2 structures (> 3.8 V), and is characterized by an upshifted reflection of the (002) peak (denoted (002')) that corresponds to a contraction of the *c*-axis.[24] This is also typically associated with peak broadening due to the formation of stacking faults from slab gliding. However, after 150 charge-discharge cycles, a minor (002') peak at ~18º was observed in both $Na_{0.66}Mn_{0.9}Mg_{0.1}O_2$ and $Na_{0.66}Mn_{0.95}Mg_{0.05}O_2$. This reflects a contraction of the interlayer space with O2-type stacking.[34–36] It is often explained as an OP4 phase that possesses alternating layers of octahedral and prismatic sites along the *c*-axis.[34] Alternatively, others have referred to it as the Z phase and is ascribed to the migration of a transition metal ions (M) into the interlayer space to form MO_4 tetrahedra, which is favored at high Na^+ vacancy. This induces short range order between the metal oxide slabs with O2 stacking.[36] The presence of the (002') peak indicates that minor irreversible phase changes occurred over long-term cycling at 4.5 $V_{cut\text{-}off}$. Differences between the $Na_{0.66}Mn_{0.9}Mg_{0.1}O_2$ and $Na_{0.66}Mn_{0.95}Mg_{0.05}O_2$ patterns were observed upon closer examination after 150 charge-discharge cycles (Figure 4C). The (102), (104), (106), and (110) peaks on $Na_{0.66}Mn_{0.95}Mg_{0.05}O_2$ appear to broaden, which we believe is associated with inhomogeneous microstrains and stacking faults in the P2 structure due to slab gliding. Thus, the *ex-situ* XRD studies confirm that the increased Mg doping extends cyclability by suppressing irreversible structural changes.

The *ex-situ* XRD patterns of $Na_{0.66}Mn_{0.95}Mg_{0.05}O_2$ after 150 and 100 cycles at 4.6 and 4.7 $V_{cut\text{-}off}$ respectively are shown in Figure S6. Peaks corresponding to the hydrated P2-phase were observed in both samples, which reflects an expanded interlayer space caused by electrolyte insertion between the transition metal oxide slabs.[37] This phase is commonly observed when charged to high voltages, due to the increased susceptibility toward electrolyte insertion at high Na^+ vacancy.[25,38] Both samples also displayed greater peak broadening, which is indicative of more stacking faults. In addition, a broad (002') peak at ~22º was observed which can be indexed as the O2-phase. This peak intensity was considerably greater for the sample cycled at 4.7 $V_{cut\text{-}off}$. These results indicate that irreversible electrolyte insertion and phase changes were largely responsible for the loss of Na^+ storage capacity. Lastly, it should be noted that significant active material dissolution was clearly observed after disassembling the cells cycled at 4.7 $V_{cut\text{-}off}$, which corresponds with the drastic evolution of the charge-discharge curves shown in Figure S4.

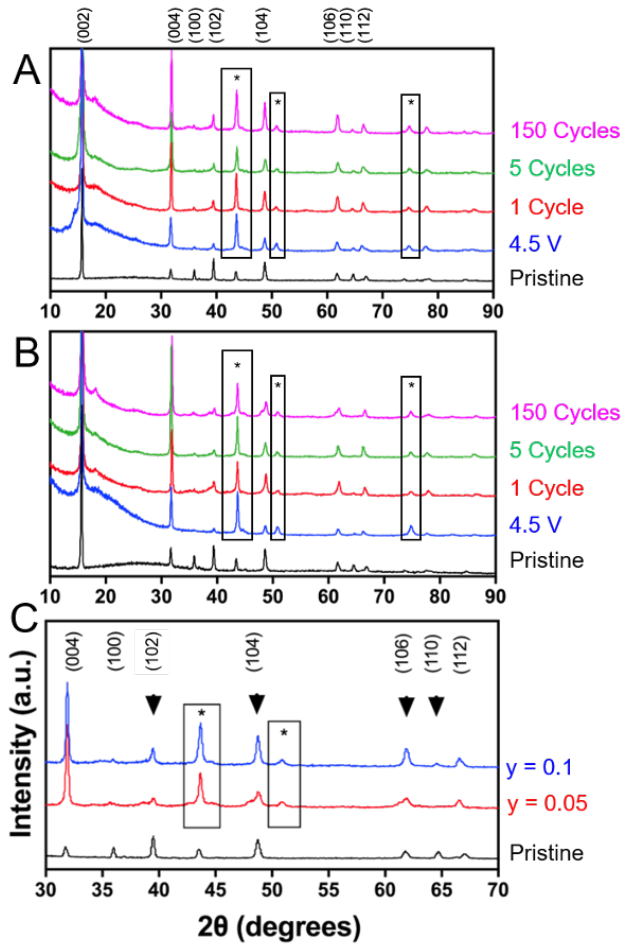

Figure 4. *Ex-situ* XRD patterns of $Na_{0.66}Mn_{1-y}Mg_yO_2$ at various stages of cycling between 2 – 4.5 V. '*' marks peaks from the stainless steel current collector. A) y = 0.1, B) y = 0.05, C) Comparison between both compositions after 150 cycles.

Conclusions

P2-$Na_{0.66}Mn_{1-y}Mg_yO_2$ was synthesized using a modified Pechini method at various Mg content (y = 0, 0.5, and 0.1) and the electrochemical performance was characterized at various upper cut-off voltages (4.5, 4.6, and 4.7 V). $Na_{0.66}Mn_{0.95}Mg_{0.05}O_2$ displayed a similar initial discharge capacity compared to $Na_{0.66}MnO_2$ with significantly improved cycle retention, due to the suppression of Na^+/vacancy ordering, Jahn-Teller distortion, and high-voltage phase transitions. $Na_{0.66}Mn_{0.9}Mg_{0.1}O_2$ showcased an improvement in cycle retention and rate capability, albeit with lower discharge capacity. At a 4.5 V cut-off, the cycle stability of the Mg-doped samples was remarkable for a layered structure reliant on the Mn^{3+}/Mn^{4+} redox. *Ex-situ* XRD characterization revealed that both $Na_{0.66}Mn_{0.95}Mg_{0.05}O_2$ and $Na_{0.66}Mn_{0.9}Mg_{0.1}O_2$ retained their pristine P2 structure after extensive cycling from 2 – 4.5 V. The small differences in cycle retention was ascribed to

the formation of stacking faults and microstrains in $Na_{0.66}Mn_{0.95}Mg_{0.05}O_2$, leading to peak broadening. At 4.6 and 4.7 V cut-offs, electrolyte insertion between the metal oxide slabs, excessive electrolyte decomposition, irreversible octahedral-related phase transitions, and active material dissolution (at 4.7 V) were major factors of irreversible capacity loss. The extraordinarily high discharge capacity of P2-$Na_{0.66}Mn_{1-y}Mg_yO_2$ when cycled at high voltage cut-offs makes it a promising cathode material for sodium-ion batteries, with opportunities to further improve its cyclability through strategies such as surface coatings, forming nanostructured composites, and incorporating ionic liquid electrolytes.

Experimental Section

Synthesis of P2-$Na_{0.66}Mn_{1-y}Mg_yO_2$

P2-$Na_{0.66}Mn_{1-y}Mg_yO_2$ was synthesized using a modified Pechini method. Stoichiometric amounts (for y = 0.05 and y = 0.1) of sodium (5% excess), manganese, and magnesium acetate (Sigma-Aldrich, Mississauga, Canada) were dissolved in distilled water (0.25 M metal ions). An equivalent volume of aqueous 0.575 M citric acid (Sigma-Aldrich) and aqueous 5 wt% poly(ethylene glycol) (number-average M_W = 8,000 Da) were added dropwise to the metal-acetate mixture. Ethylene glycol (3 mL, Sigma-Aldrich) and concentrated nitric acid (1 mL, 70%, Sigma-Aldrich) were then added dropwise to the mixture, which was stirred at 110˚C for ~ 4 h. The resulting gel precursor was dried overnight at 110˚C, then pre-calcined at 400˚C for 4 h in a muffle furnace (Thermo Scientific, Mississauga, Canada) to remove organic residue. Finally, the resulting powder was ground and sintered at 850˚C for 12 hr in a tube furnace (Thermo Scientific) under open air. The final P2-$Na_{0.66}Mn_{1-y}Mg_yO_2$ powder was stored in a vacuum oven to avoid water ingress and oxidation.

Characterization of P2-$Na_{0.66}Mn_{1-y}Mg_yO_2$ Particles

The phase purity of the active material was assessed using powder X-ray diffraction (XRDMiniflex 600, Rigaku, Japan) with Cu K_α radiation (λ = 1.5406 nm). The morphology of the particles was observed using scanning electron microscopy (SEM, LEO Zeiss 1550, Switzerland) using a 20 kV acceleration voltage and a working distance between 8 – 9 mm. Rietveld refinement was conducted on MAUD software[39] using COD ID: 1525855[40] as a reference. Inductively coupled plasma atomic emission spectroscopy (ICP-AES) was conducted after dissolution of metal oxides in Aqua regia (4:1 concentrated HCl:HNO_3 (v/v)).

Preparation of P2-$Na_{0.66}Mn_{1-y}Mg_yO_2$ Electrode

The electrode was prepared by grinding a slurry of 70 wt% active material, 20% conductive carbon black (Ketjenblack, Lion Specialty Chemical Co., Japan), and 10% PTFE-acetylene black binder in ethanol using a mortar and pestle. The electrode film was pressed (~10,000 kPa) onto a 15 mm diameter stainless steel mesh and dried overnight at 80˚C in a vacuum oven. The active material loading was 6 mg cm^{-2}.

Electrochemical Characterization of P2-$Na_{0.66}Mn_{1-y}Mg_yO_2$ Electrode

The electrochemical performance of the P2-$Na_{0.66}Mn_{1-y}Mg_yO_2$ electrode was assessed by assembling CR2032 coin cells in an argon-filled glove box (O_2 and H_2O ppm < 0.5, MBRAUN, Stratham, NH, USA) using a pure sodium foil (Sigma-Aldrich) as the counter electrode, a polypropylene separator (Celgard 2400, Charlotte, NC, USA), and an electrolyte comprised of 1 M $NaClO_4$ dissolved in 1:1:0.1 ethylene carbonate:diethyl carbonate:fluoroethylene carbonate (Sigma-Aldrich) by volume. Charge-discharge studies were carried out at ambient temperature using a CT2001A LANDt battery testing system (Wuhan, China). Electrochemical impedance spectroscopy (EIS) measurements (Gamry Instruments, Warminster, PA, USA) were conducted from 1 MHz to 100 mHz at a discharged state (~2 V).

Acknowledgements

The authors gratefully acknowledge Ruohan Jiang for acquiring the SEM images and Yanfei Zhu for conducting the ICP-AES tests. Financial support from the Natural Sciences and Engineering Research Council of Canada (NSERC), Henan Normal University, and the University of Waterloo is acknowledged. This work was supported by the 111 Project (No. D17007). Tyler Or was personally supported through the NSERC Canada Graduate Scholarships-Master's Program.

References

[1] H. Vikström, S. Davidsson, M. Höök, *Appl. Energy* **2013**, *110*, 252–266.

[2] J.-Y. Hwang, S.-T. Myung, Y.-K. Sun, *Chem. Soc. Rev.* **2017**, *46*, 3529–3614.

[3] X. Xiang, K. Zhang, J. Chen, *Adv. Mater.* **2015**, *27*, 5343–5364.

[4] C. Delmas, C. Fouassier, P. Hagenmuller, *Phys. B+C* **1980**, *99*, 81–85.

[5] Y. Wang, R. Xiao, Y.-S. Hu, M. Avdeev, L. Chen, *Nat. Commun.* **2015**, *6*, 6954.

[6] A. Caballero, L. Hernán, J. Morales, L. Sánchez, J. Santos Peña, M. A. G. Aranda, *J. Mater. Chem.* **2002**, *12*, 1142–1147.

[7] D. Su, C. Wang, H. J. Ahn, G. Wang, *Chem. - A Eur. J.* **2013**, *19*, 10884–10889.

[8] J. Billaud, G. Singh, A. R. Armstrong, E. Gonzalo, V. Roddatis, M. Armand, T. Rojo, P. G. Bruce, *Energy Environ. Sci.* **2014**, *7*, 1387–1391.

[9] D. Buchholz, C. Vaalma, L. G. Chagas, S. Passerini, *J. Power Sources* **2015**, *282*, 581–585.

[10] N. Sharma, N. Tapia-Ruiz, G. Singh, A. R. Armstrong, J. C. Pramudita, H. E. A. Brand, J. Billaud, P. G. Bruce, T. Rojo, *Chem. Mater.* **2015**, *27*, 6976–6986.

[11] R. J. Clément, J. Billaud, A. Robert Armstrong, G. Singh, T. Rojo, P. G. Bruce, C. P. Grey, *Energy Environ. Sci.* **2016**, *9*, 3240–3251.

[12] Q. C. Wang, J. K. Meng, X. Y. Yue, Q. Q. Qiu, Y. Song, X. J. Wu, Z. W. Fu, Y. Y. Xia, Z. Shadike, J. Wu, et al., *J. Am. Chem. Soc.* **2019**, *141*, 840–848.

[13] Y. Huang, Z. Yan, W. Luo, Z. Hu, G. Liu, L. Zhang, X. Yang, M. Ou, W. Liu, L. Huang, et al., *Energy Storage Mater.* **2020**, *29*, 182–189.

[14] Y. Lv, X. Cheng, W. Qiang, B. Huang, *J. Power Sources* **2020**, *450*, 227718.

[15] N. Yabuuchi, R. Hara, K. Kubota, J. Paulsen, S. Kumakura, S. Komaba, *J. Mater. Chem. A* **2014**, *2*, 16851–16855.

[16] U. Maitra, R. A. House, J. W. Somerville, N. Tapia-Ruiz, J. G. Lozano, N. Guerrini, R. Hao, K. Luo, L. Jin, M. A. Pérez-Osorio, et al., *Nat. Chem.* **2018**, *10*, 288–295.

[17] K. Kaliyappan, T. Or, Y. Deng, Y. Hu, Z. Bai, Z. Chen, *Adv. Funct. Mater.* **2020**, 1910251.

[18] R. J. Clément, J. Billaud, A. Robert Armstrong, G. Singh, T. Rojo, P. G. Bruce, C. P. Grey, *Energy Environ. Sci.* **2016**, *9*, 3240–3251.

[19] K. Kaliyappan, W. Xiao, K. R. Adair, T.-K. Sham, X. Sun, *ACS Omega* **2018**, *3*, 8309–8316.

[20] H. Xia, H. Wang, W. Xiao, L. Lu, M. O. Lai, *J. Alloys Compd.* **2009**, *480*, 696–701.

[21] T. Zaki, K. I. Kabel, H. Hassan, *Ceram. Int.* **2012**, *38*, 4861–4866.

[22] F. Croce, A. D' Epifanio, J. Hassoun, A. Deptula, T. Olczac, B. Scrosati, *Electrochem. Solid-State Lett.* **2002**, *5*, A47.

[23] R. D. Shannon, C. T. Prewitt, *Acta Crystallogr. Sect. B Struct. Crystallogr. Cryst. Chem.* **1969**, *25*, 925–946.

[24] Z. Lu, J. R. Dahn, *J. Electrochem. Soc.* **2001**, *148*, A1225.

[25] P.-F. Wang, Y. You, Y.-X. Yin, Y.-S. Wang, L.-J. Wan, L. Gu, Y.-G. Guo, *Angew. Chemie Int. Ed.* **2016**, *55*, 7445–7449.

[26] G. Singh, N. Tapia-Ruiz, J. M. Lopez del Amo, U. Maitra, J. W. Somerville, A. R. Armstrong, J. Martinez de Ilarduya, T. Rojo, P. G. Bruce, *Chem. Mater.* **2016**, *28*, 5087–5094.

[27] X. Wu, J. Guo, D. Wang, G. Zhong, M. J. McDonald, Y. Yang, *J. Power Sources* **2015**, *281*, 18–26.

[28] Y. You, A. Manthiram, *Adv. Energy Mater.* **2018**, *8*, 1701785.

[29] K. Chayambuka, G. Mulder, D. L. Danilov, P. H. L. Notten, *Adv. Energy Mater.* **2018**, *8*, 1800079.

[30] L. G. Chagas, D. Buchholz, L. Wu, B. Vortmann, S. Passerini, *J. Power Sources* **2014**, *247*, 377–383.

[31] I. Saadoune, A. Maazaz, M. Ménétrier, C. Delmas, *J. Solid State Chem.* **1996**, *122*, 111–117.

[32] Z.-Y. Li, R. Gao, J. Zhang, X. Zhang, Z. Hu, X. Liu, *J. Mater. Chem. A* **2016**, *4*, 3453–3461.

[33] A. Mendiboure, C. Delmas, P. Hagenmuller, *J. Solid State Chem.* **1985**, *57*, 323–331.

[34] N. Yabuuchi, M. Kajiyama, J. Iwatate, H. Nishikawa, S. Hitomi, R. Okuyama, R. Usui, Y. Yamada, S. Komaba, *Nat. Mater.* **2012**, *11*, 512–517.

[35] B. Mortemard de Boisse, D. Carlier, M. Guignard, L. Bourgeois, C. Delmas, *Inorg. Chem.* **2014**, *53*, 11197–11205.

[36] E. Talaie, V. Duffort, H. L. Smith, B. Fultz, L. F. Nazar, *Energy Environ. Sci.* **2015**, *8*, 2512–2523.

[37] D. Buchholz, L. G. Chagas, C. Vaalma, L. Wu, S. Passerini, *J. Mater. Chem. A* **2014**, *2*, 13415–13421.

[38] P. Hou, Y. Sun, F. Li, Y. Sun, X. Deng, H. Zhang, X. Xu, L. Zhang, *Nanoscale* **2019**, *11*, 2787–2794.

[39] L. Lutterotti, *Nucl. Instruments Methods Phys. Res. Sect. B Beam Interact. with Mater. Atoms* **2010**, *268*, 334–340.

[40] Z. Lu, J. R. Dahn, *J. Electrochem. Soc.* **2001**, *148*, A237.

10.1002/celc.202000414

Table of Contents Graphic

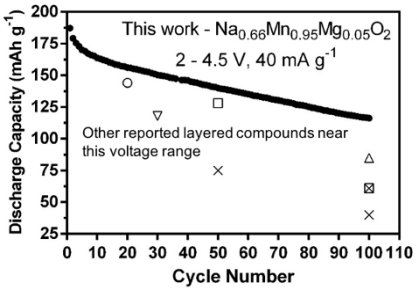

In this work, we systematically test and characterize the performance and behavior of P2-$Na_{0.66}Mn_{1-y}Mg_yO_2$ at various Mg doping compositions and upper cut-off voltages. The failure mechanisms typically observed at high voltage cycling are assessed. The material demonstrates promise as a high capacity and environmentally benign cathode for sodium-ion batteries.